

# Spin-Selective Full-Dimensional Manipulation of Optical Waves with Chiral Mirror

Zhancheng Li, Wenwei Liu, Hua Cheng,\* Duk-Yong Choi, Shuqi Chen,\* and Jianguo Tian

Realizing arbitrary manipulation of optical waves, which still remains a challenge, plays a key role in the implementation of optical devices with on-demand functionalities. However, it is hard to independently manipulate multiple dimensions of optical waves because the optical dimensions are basically associated with each other when adjusting the optical response of the devices. Here, the concise design principle of a chiral mirror is utilized to realize the full-dimensional independent manipulation of circular-polarized waves. By simply changing three structural variables of the chiral mirror, the proposed design principle can arbitrarily and independently empower the spin-selective manipulation of amplitude, phase, and operation wavelength of circular-polarized waves with a large modulation depth. This approach provides a simple solution for the realization of spin-selective full-dimensional manipulation of optical waves and shows ample application possibilities in the areas of optical encryption, imaging, and detection.

Realizing the spin-selective multidimensional manipulation of optical waves plays a key role in many research fields of optics and photonics, such as quantum optics, spin photonics,

and integrated optics.<sup>[1–7]</sup> However, the weak chiral optical responses in natural materials prevent them from being used in the implementation of spin-selective optical wave manipulation.<sup>[8]</sup> Metasurfaces, which are planar arrays composed of subwavelength artificial nanostructures, have received a burgeoning amount of interest in the field of spin photonics due to their significantly enhanced chiral optical responses compared with natural materials.<sup>[9–12]</sup> Recently, spin-selective focusing,<sup>[13,14]</sup> hologram,<sup>[15,16]</sup> transmission,<sup>[17–19]</sup> asymmetric transmission,<sup>[20,21]</sup> anomalous refraction,<sup>[22,23]</sup> and multifunction integration<sup>[24–29]</sup> have been successively implemented with metasurfaces. These approaches indicate that the metasurfaces with giant chiral optical response

provide an effective platform for the implementation of spin-selective manipulation of optical waves.

Chiral mirrors are exotic spin-selective reflectors based on metasurfaces,<sup>[30–32]</sup> one type of which can reflect optical waves in one circular polarization state without polarization change while absorb optical waves in the other circular polarization state.<sup>[32]</sup> Chiral mirrors have been treated as an effective approach for the realization of spin-selective near-field enhancement,<sup>[33]</sup> absorption,<sup>[34–37]</sup> and circularly polarized light detection.<sup>[38]</sup> By utilizing the geometric phase, recent advances in chiral mirrors also show that they are good alternatives for the realization of spin-selective phase manipulation of optical waves.<sup>[39–41]</sup> However, the implementation of the diverse chiral optical functionalities by metasurfaces does not only require phase manipulation of optical waves. Spin-selective full and independent amplitude and phase manipulation of optical waves with a large and continuous wavelength agility, namely spin-selective full-dimensional manipulation of optical waves, is more highly desirable. To realize the spin-selective full-dimensional manipulation of optical waves, there are still some critical issues need to be solved. Firstly, it is challenging to realize independent manipulation of different dimensions of optical waves, because they are always associated with each other when varying the structural parameters of the metasurfaces.<sup>[3]</sup> Further, how to realize a large modulation depth for full-dimensional manipulation of optical waves by finite variation of structural parameters of metasurfaces still needs to be solved. It is worth mentioning that even these issues might be solved by utilizing deep-learning technology,<sup>[42,43]</sup> the data collection process is time consuming and the method itself lacks physical guidance.

Dr. Z. Li, Dr. W. Liu, Prof. H. Cheng, Prof. S. Chen, Prof. J. Tian  
The Key Laboratory of Weak Light Nonlinear Photonics  
Ministry of Education  
School of Physics and TEDA Institute of Applied Physics  
Renewable Energy Conversion and Storage Center  
Nankai University  
Tianjin 300071, China  
E-mail: hcheng@nankai.edu.cn; schen@nankai.edu.cn

Prof. D.-Y. Choi  
Laser Physics Centre  
Research School of Physics  
Australian National University  
Canberra ACT 2601, Australia

Prof. D.-Y. Choi  
College of Information Science and Technology  
Jinan University  
Guangzhou 510632, China

Prof. S. Chen  
The Collaborative Innovation Center of Extreme Optics  
Shanxi University  
Taiyuan, Shanxi 030006, China

Prof. S. Chen  
The Collaborative Innovation Center of Light  
Manipulations and Applications  
Shandong Normal University  
Jinan 250358, China

 The ORCID identification number(s) for the author(s) of this article can be found under <https://doi.org/10.1002/adma.201907983>.

DOI: 10.1002/adma.201907983

Here, we provide a simple design principle of chiral mirror to realize the spin-selective full-dimensional manipulation of optical waves. Our approach reveals the direct relationships between the structural parameters of the designed chiral mirrors and three independent optical dimensions. By simply changing three structural variables of the two chiral mirrors with opposite spin-selective responses, the proposed design principle can arbitrarily and independently empower the spin-selective manipulation of amplitude, phase, and operation wavelength of the circular-polarized waves with a large modulation depth. With experimental validation, we further prove that the proposed chiral mirrors can be used not only in the applications based on spin-selective phase manipulation of optical waves, such as wavefront manipulation, but also in the areas of optical encryption, imaging, and detection. Our work can overcome the drawbacks in previous chiral mirrors and provides a simple solution for the implementation of spin-selective full-dimensional manipulation of optical waves.<sup>[30–41]</sup>

Figure 1a is a schematic that shows the spin-selective optical response of a designed aluminum chiral mirror. It can reflect right-handed circular polarized (RCP) waves without polarization change while absorb left-handed circular polarized (LCP) waves. The proposed chiral mirror is a metal-insulator-metal design composed of a ground aluminum layer, a SiO<sub>2</sub> spacer layer and a top layer of aluminum nanostructures. The structural parameters of a unit cell of the chiral mirror are shown in Figure 1b, where the periods  $P = P_x = P_y = 650$  nm. The dimensions of the aluminum nanostructures are  $w = 70$  nm,  $r_1 = 230$  nm,  $r_2 = 160$  nm, and  $t_1 = 70$  nm, respectively. The thicknesses of the SiO<sub>2</sub> spacer layer and the ground aluminum layer are  $t_2 = 180$  nm and  $t_3 = 200$  nm, respectively. Figure 1c shows three structural variables in a unit cell of the chiral mirror: the length of the short arc (represented by angle  $\alpha$ ), the length of the symmetrical long arc (represented by angle  $\beta$ ) and the orientation angle of the nanostructures along the z-axis (represented by angle  $\theta$ ). Spin-selective manipulation of amplitude, phase, and operation wavelength of optical waves can be realized by changing the three structural parameters near-independently.

First, we propose two chiral mirrors with opposite chiral optical responses to realize the spin-selective reflection of LCP and RCP waves, respectively. Figure 2 shows the simulated and measured modular square  $r_{ij} = |R_{ij}|^2$  (the subscript “i” and “j” indicate the polarization state of the reflected and incident optical waves, respectively) of the reflection coefficients and the corresponding calculated reflection difference  $\Delta r = r_{\text{LCP}} - r_{\text{RCP}}$  for two chiral mirrors with structural variables  $\alpha = 45^\circ$ ,  $\beta = 80^\circ$ , and  $\theta = 0^\circ$ . Chiral mirror in Figure 2b can be obtained by rotating the aluminum nanostructure in Figure 2a 180° along y-axis. Simulated results in Figures 2a–c indicate that the proposed chiral mirrors can realize spin-selective reflection of optical waves around 1384 nm with reflection difference over 78% and a near-perfect extinction of one circular-polarized illumination. These two chiral mirrors have opposite spin-selective optical responses, which can be regarded as enantiomorph (A and B). The measured results in Figure 2d,e are in good agreement with the simulated results, even there exists a minute wavelength discrepancy, that is ascribed to the small structural differences between the designed and fabricated nanostructures. We further analyze the variation of the spin-selective optical response of the proposed chiral mirrors at various incident angles (Figure S1, Supporting Information). The spin-selective optical responses of the proposed chiral mirrors remain unchanged when incident angle is below to 30°. We also analyze the influence of structural parameters ( $P$ ,  $w$ ,  $r_1$ ,  $r_2$ ,  $t_1$ , and  $t_2$ ) on the spin-selective optical responses in Figure S2, Supporting Information. The optical responses of the proposed chiral mirrors are stable when the structural parameters are varying in a certain range. It is worth mentioning that, a significant change of the spacer layer thickness  $t_2$  will remarkably affect the resonance strength of the aluminum nanostructures, because the resonance of the aluminum nanostructures is enhanced by the multiple reflections of optical waves that is induced by the metal-insulator-metal configuration (Figure S3, Supporting Information).

The spin-selective reflections in the proposed chiral mirrors originate from the spin-selective excitation of a pair of

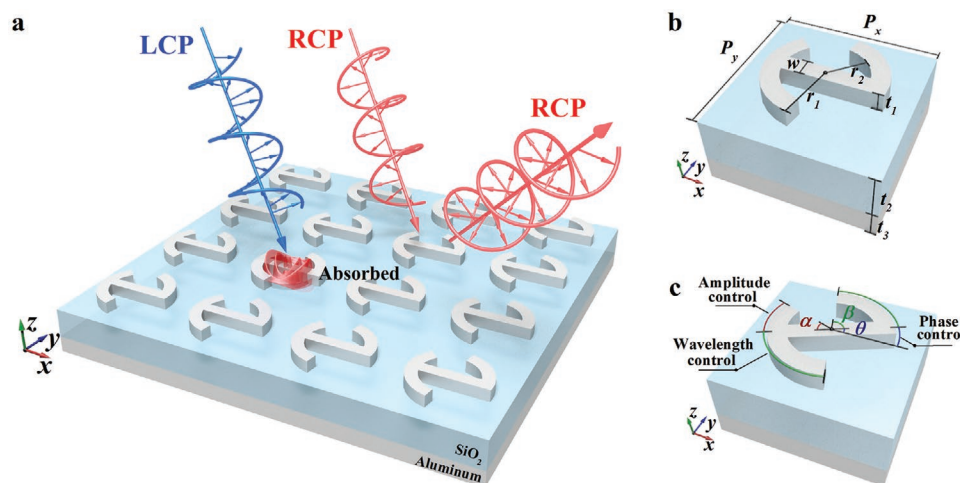


**Figure 1.** Schematic illustrating the optical response, design principle, and structural variables of the designed chiral mirror. a) Schematic of the spin-selective reflection in aluminum chiral mirror. b) An illustration of the structural parameters of a unit cell in chiral mirror. c) Structural variables in a unit cell for the realization of full-dimensional manipulation of circular-polarized waves.

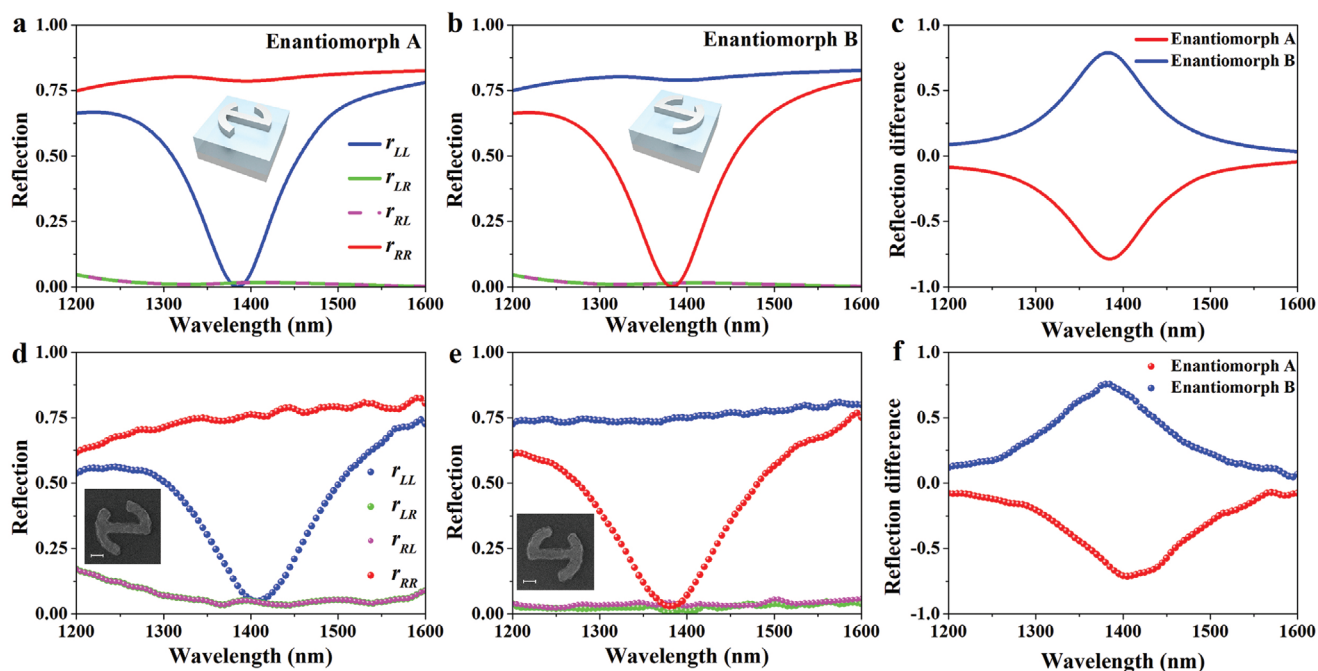


**Figure 2.** Simulated and measured reflection spectra for the designed chiral mirrors. a–c) Simulated modular square  $r_{ij} = |R_{ij}|^2$  of the reflection coefficients for the designed chiral mirrors: a) the enantiomorph A, b) the enantiomorph B, and c) the corresponding calculated reflection difference  $\Delta r = r_{LCP} - r_{RCP}$  (Insets: schematic of a basic unit cell of the enantiomorphs A and B). d–f) Experimentally measured modular square  $r_{ij} = |R_{ij}|^2$  of the reflection coefficients for the designed chiral mirrors: d) the enantiomorph A, e) the enantiomorph B, and f) the corresponding experimental reflection difference  $\Delta r = r_{LCP} - r_{RCP}$  (Insets: SEM images of a basic unit cell of the fabricated enantiomorph A and the fabricated enantiomorph B, scale bar: 100 nm).

antiparallel currents within the nanostructures, as shown in **Figure 3a**. The excitation of antiparallel currents in the nanostructures (represented by the red and blue arrows) results in not only the minimization of electric dipole response but also the generation of a pair of parallel magnetic dipoles along the wave propagation direction, which lead to the vanishingly small far-field emission. To further make a quantitative analysis, we calculated and compared the scattering power of multipole excitations by utilizing the electromagnetic multipole expansion method.<sup>[44–47]</sup> As shown in **Figure 3b**, the calculated results validate that the main multipole excitation in the enantiomorph A under LCP illumination is the magnetic dipole ( $M$ ) with the main component in the  $z$  direction ( $M_z$ ) (**Figure 3c**), which are in good agreement with the simulated results in **Figure 3a**. While for RCP illumination, the main multipole excitation in the enantiomorph A is electric dipole ( $P$ ) with main component in  $y$  direction ( $P_y$ ) (**Figure 3c**). For the enantiomorph B, the situation is exactly opposite. Thus, the spin-selective reflections in the proposed chiral mirrors are ascribed to the spin-selective excitation of magnetic dipoles in wave propagation direction and minimization of electric dipole perpendicular to wave propagation direction, resulting in the vanishingly small far-field emission.

The spin-selective reflections in the proposed chiral mirrors are attributed to the generation of a pair of antiparallel currents within the nanostructures. The antiparallel currents within the nanostructures can be related to two electric dipoles with phase delay of  $\pi$ . Thus, the proposed nanostructures can be equivalent to the optical nanoantenna, whose second-order resonance has been excited. The excitation of the second-order resonance

in the proposed nanostructure is attributed to the symmetry breaking of the nanostructure by adding the short arc structure. Moreover, the far-field scattering  $E_s$  associated with the electric dipole in metasurfaces can be expressed as:<sup>[46]</sup>

$$\mathbf{E}_s = -\frac{i\mu_0 k c^2}{2A^2} \mathbf{P}_{\parallel} = -\frac{i\mu_0 k c^2}{2A^2} (\mathbf{P}_x \mathbf{i} + \mathbf{P}_y \mathbf{j}) \quad (1)$$

where  $A$  is the area of the unit cell, and  $P_x$  and  $P_y$  can be expressed as  $P_{\alpha} = \frac{1}{i\omega} \int d^3 r J_{\alpha}$ . By varying the length of the short arc structure, both  $P_x$  and  $P_y$  can be manipulated, which means that the length of the short arc is directly associated with the efficiency of the spin-selective reflection in the proposed chiral mirrors. The scattering intensity of  $P_x$  and  $P_y$  will decrease and increase with the increasing of the angle  $\alpha$  (**Figure S4**, Supporting Information), respectively. The sum of the scattering intensity of  $P_x$  and  $P_y$  reaches minimum value when  $\alpha = 45^\circ$ . Therefore, we can manipulate the amplitude of the spin-selective reflection by controlling the angle  $\alpha$ , as shown in **Figures 4a–c**. The simulated results also validate that we can effectively manipulate the amplitude of LCP reflected waves at operation wavelength by changing the angle  $\alpha$  while keeping the reflection intensity of RCP waves in constant. Since the current density within the short arc structure is quite weak for RCP waves, which can be validated by the distribution of the power loss density in **Figure 3a**, the variation of the angle  $\alpha$  has a limited influence on the reflection intensity of RCP waves. In addition, the range of amplitude manipulation is from 0 ( $\alpha = 45^\circ$ ) to 0.87 ( $\alpha = 15^\circ$ ) at 1384 nm. Moreover, the

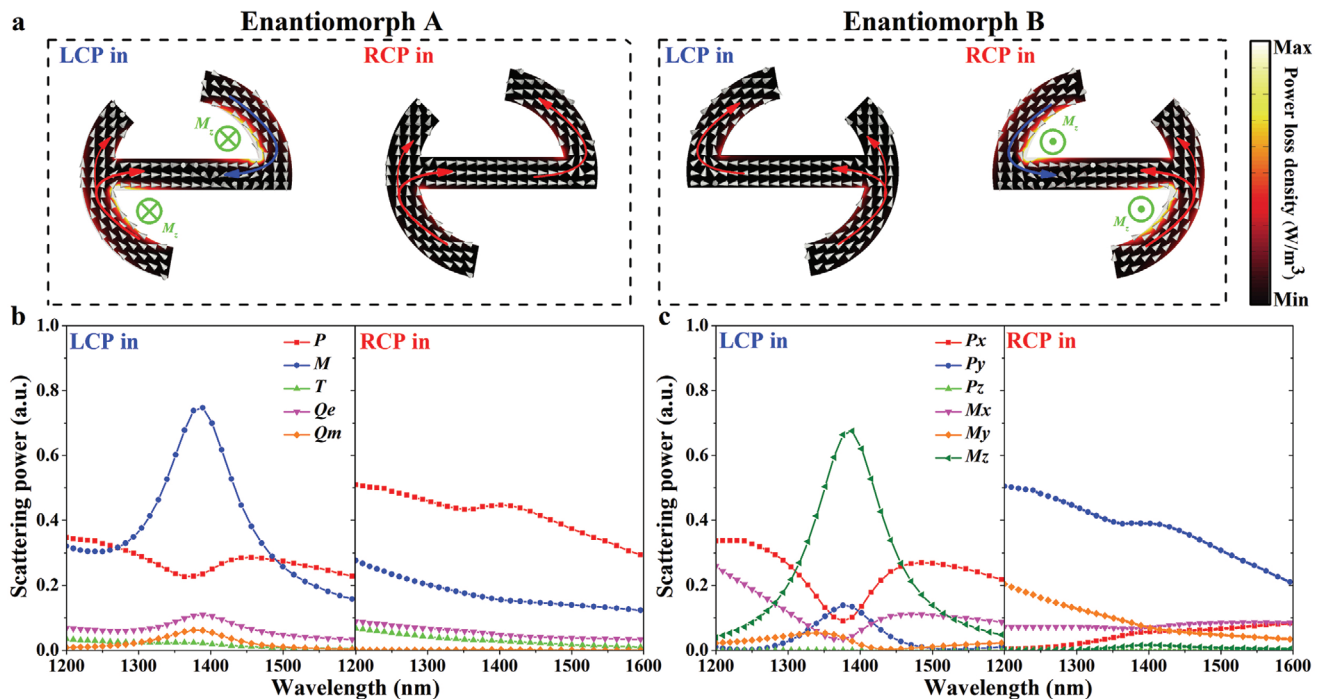


**Figure 3.** The physical mechanisms of the spin-selective reflection in the designed chiral mirrors. a) Simulated results of the direction of the current flow (white arrow) and the distribution of the power loss density in enantiomorph A and B (on the middle section of the nanostructure in a unit cell) at 1384 nm under LCP and RCP illuminations. b) Calculated multipolar decomposition of scattering spectra of the enantiomorph A in terms of electric dipole ( $P$ ), magnetic dipole ( $M$ ), toroidal dipole ( $T$ ), electric quadrupole ( $Q_e$ ), and magnetic quadrupole ( $Q_m$ ) under LCP and RCP illuminations. c) Calculated results of the component of electric dipole ( $P$ ) and magnetic dipole ( $M$ ) under LCP and RCP illuminations.

second-order resonance of a nanoantenna with structural symmetry breaking can be excited when the equivalent wavelength of optical waves equals to the length of the nanoantenna, which means that the operation wavelength of the nanoantenna is proportional to its length. In a similar way, the operation wavelength  $\lambda_0$  of the proposed chiral mirrors is proportional to the sum of the length of the long arc and the horizontal nanorod:

$$\lambda_0 \propto (r_1 + r_2)\beta + 2r_2 \quad (2)$$

Thus, the operation wavelength can be manipulated by changing the length of the long arc, in other word, the angle  $\beta$ . As shown in Figures 4d–f, the operation wavelength can be effectively controlled from 1000 nm to 2000 nm by changing the angle  $\beta$  from  $45^\circ$  to  $125^\circ$  while keeping the value of  $r_{LL}$  constant. Moreover, the variation of the operation wavelength has a linear relationship with the changing of the angle  $\beta$ , which is in good agreement with the above prediction. When the angle  $\beta > 115^\circ$ , the relationship between the operation wavelength and the angle  $\beta$  is slightly changed. This can be attributed to the extra near-field interaction induced by the narrow gap between the short and long arc structures. Since the current flows in the two long arc structures are opposite and their integral are cancelled out (Figure S5, Supporting Information), the variation of the angle  $\beta$  almost has no effect on the amplitude of the spin-selective reflection. Furthermore, the designed chiral mirrors can not only realize the spin-selective reflection of optical waves, but also change their spins ( $r_{LL}$  or  $r_{RR}$  are not equal to zero while  $r_{LR}$  and  $r_{RL}$  are equal to zero). Thus, we can realize the phase manipulation of optical waves by utilizing

the geometric phase: when a circular-polarized optical wave is reflected by a nanostructure with a rotation angle of  $\varphi$ , an extra phase of  $\pm 2\varphi$  will be added to the reflected wave with opposite spin.<sup>[22]</sup> By changing the orientation angle  $\theta$  from 0 to  $\pi$ , we can manipulate the phase of the reflected waves from 0 to  $2\pi$ , as shown in Figures 4g–i, while the amplitudes of the reflected waves keep constant. It is worth mentioning that the variations of  $\alpha$  and  $\beta$  will cause the change of the resonance phase, thus extra geometric phase needs to be added to make a compensation to realize the spin-selective independent manipulation of amplitude, phase and operation wavelength of optical waves. Overall, we can realize full-dimensional manipulation of LCP and RCP optical waves with a large modulation depth by using two chiral mirror designs and changing the three structural variables. Compared with previous works in the research area of chiral mirrors,<sup>[32–41]</sup> our approach can be used not only in the applications based on spin-selective phase manipulation of optical waves, such as wavefront manipulation (Figure S6, Supporting Information), but also in the areas of optical encryption, imaging, and detection. We further design and complete a series of experimental measurements to prove the ample application possibilities of our approach.

With the feature of the spin-selective amplitude and operation wavelength manipulation of optical waves, the proposed chiral mirrors can be utilized to realize the spin- and wavelength-encoded imaging with dual outputs. First, we experimentally validated the spin-encoded imaging by designing the spin-encoded quick response (QR) code composed of QR code A and B in Figure 5a. The designed QR code is composed of four

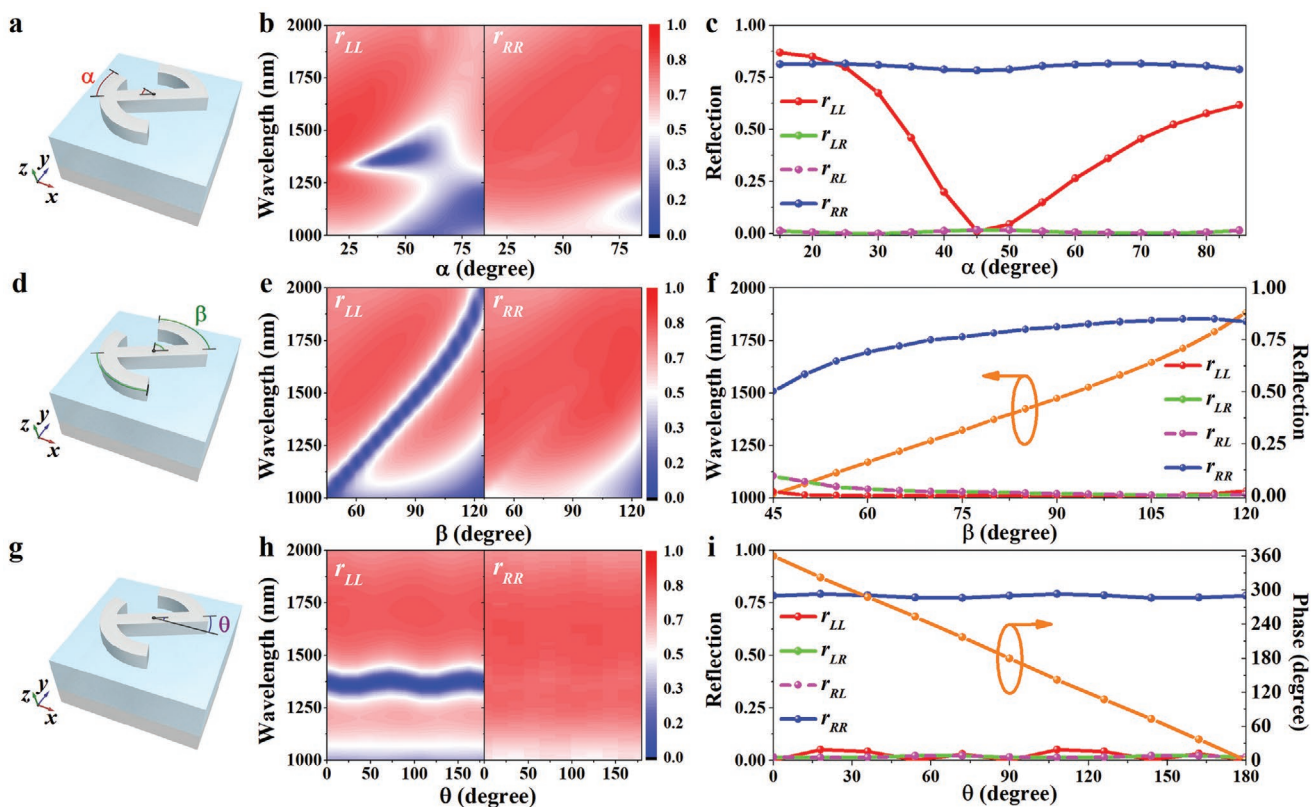


**Figure 4.** Full-dimensional independent manipulation of circular-polarized waves with the changing of three structural variables. a) Schematic of the structural variable  $\alpha$ . b) The variation of  $r_{LL}$  and  $r_{RR}$  of the enantiomorph A with the changing of  $\alpha$ . c) The variation of the modular square of the reflection coefficients for the enantiomorph A with the changing of  $\alpha$  at 1384 nm. d) Schematic of the structural variable  $\beta$ . e) The variation of  $r_{LL}$  and  $r_{RR}$  of the enantiomorph A with the changing of  $\beta$ . f) The variation of the working wavelength and the corresponding modular square of the reflection coefficients for the enantiomorph A with the changing of  $\beta$ . g) Schematic of the structural variable  $\theta$ . h) The variation of  $r_{LL}$  and  $r_{RR}$  of the enantiomorph A with the changing of  $\theta$ . i) The variation of the modular square of the reflection coefficients for the enantiomorph A and the variation of the phase of the reflection coefficients  $R_{RR}$  with the changing of  $\theta$  at 1370 nm. The variation of  $r_{LR}$  and  $r_{RL}$  are not shown in (b,e,h) because they are close to zero at operation wavelength.

basic structures (or unit cells) #1 to #4. Structures #2 and #3 are enantiomorph A and B, respectively. Structure #1 is obtained from structure #2 by deleting the aluminum nanostructure on the top layer, and structure #4 is obtained from structure #2 by deleting the short arc part of the nanostructure (Figure S7, Supporting Information). The optical responses of structures #1 and #4 are as same as a normal mirror and a handedness-preserving mirror in a broad bandwidth, respectively. With these four basic structures, we can realize a 2-bits spin-encoded imaging around the operation wavelength of the chiral mirrors. The design principle of the spin-encoded QR code is shown in Figure 5a, for example, we put structure #1 in the area that is black in both QR code A and B. QR code A and B present information for the words “metasurfaces” and “chirality”, respectively. The scanning electron microscopy (SEM) image of the designed spin-encoded QR code is shown in Figure 5b. A bromine tungsten lamp is utilized for the illumination, with different wavelength filters to acquire clear images. Figure 5c shows the experimental results of the spin-encoded QR code with different incident polarization states and detection states at the wavelength of 1400 and 1500 nm, which are in good agreement with the designed ones in Figure 5a. The experimental results indicate that the QR code can be validated

under LCP illumination and detection or RCP illumination and detection (“LCP/LCP” or “RCP/RCP”) around the operation wavelength. When under LCP or RCP illumination and without special detection of polarization (“LCP/—” or “RCP/—”) around operation wavelength, or when under “LCP/LCP” or “RCP/RCP” illumination and detection away from the operation wavelength, the designed QR code cannot be identified. In addition, for broadband illumination, the QR code cannot be observed even under specific illumination and detection states (Figure S7, Supporting Information). Thus, the spin-encoded imaging based on the proposed chiral mirrors is a good alternative for optical encryption.

Because the operation wavelength of the proposed chiral mirrors can be easily tailored, the spin- and wavelength-encoded imaging can be further implemented. We proposed and validated the spin- and wavelength-encoded imaging with dual outputs in Figure 5d,e. The designed image is also composed of four basic structures #1, #4, #5, and #6. The structures #5 and #6 are enantiomorph A with  $\beta = 68^\circ$  and  $\beta = 85^\circ$ , respectively (Figure S8, Supporting Information). With these four basic structures, we can realize a spin- and wavelength-encoded imaging with dual outputs under LCP illumination and detection. Figure 5e shows the experimental results

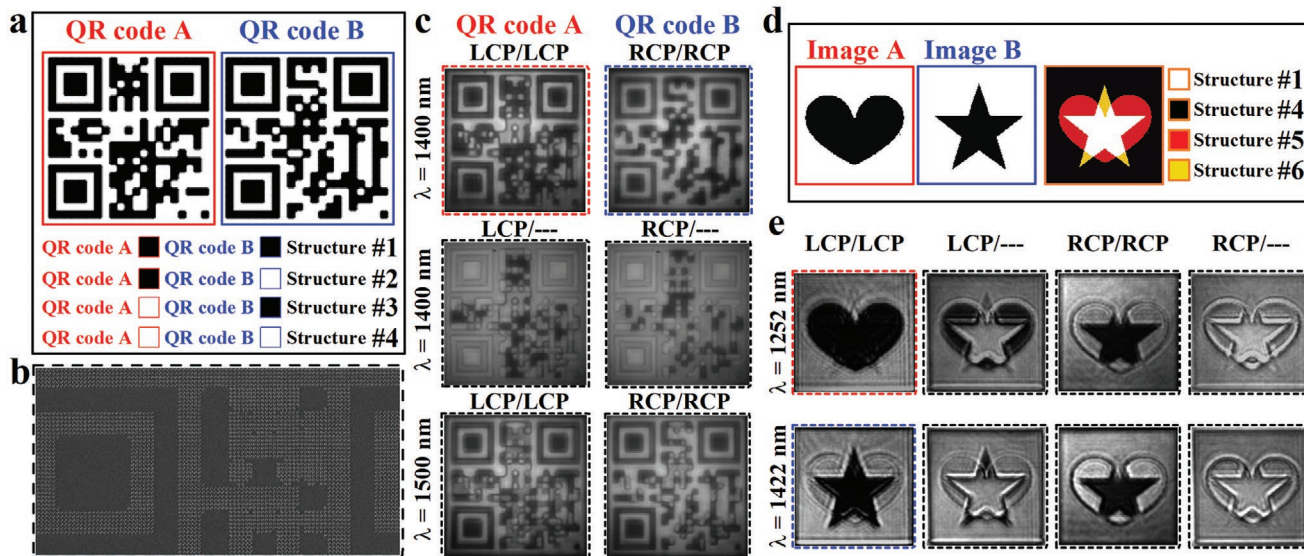


**Figure 5.** Spin- and wavelength-encoded imaging with the designed chiral mirrors. a) Design schematic of the spin-encoded imaging of two QR codes. b) SEM image of part of the fabricated spin-encoded QR code, which has 140 pixels in both  $x$ - and  $y$ -directions and each pixel consists of one of the four basic unit cells. c) Experimental results of the spin-encoded QR code under illumination and detection with different polarization states at wavelength of 1400 and 1500 nm. “LCP/LCP” (“RCP/RCP”) indicates under LCP (RCP) illumination and with LCP (RCP) detection. “LCP/—” (“RCP/—”) indicates under LCP (RCP) illumination and without special polarization detection. d) Design schematic of a spin- and wavelength-encoded image, which has 140 pixels in both  $x$ - and  $y$ -directions, and each pixel consists of one of the four basic unit cells. e) Experimental results of the spin- and wavelength-encoded imaging with different illumination and detection states at wavelength of 1252 and 1422 nm.

of the spin- and wavelength-encoded imaging with different illumination and detection states. The experimental results verify that the designed sample can display the heart- and star-shaped images under LCP illumination and detection at 1252 and 1422 nm, respectively. While with LCP illumination and without special detection of polarization, the designed image cannot be observed at two designed wavelengths. For RCP illumination, however, both designs give the same image at two wavelengths regardless of RCP detection. The boundaries between different types of unit cells exist light diffraction and interference as these images were captured under the illumination of a supercontinuum laser, which can be addressed by utilizing incoherent light source (Figure S8, Supporting Information). Overall, our approach provides an effective way for the implementation of spin- and wavelength-encoded imaging with a high degree of secrecy.

One of the outstanding advantages of our approach is that we can realize the spin-selective amplitude manipulation with a large modulation depth by only changing the structural variable  $\alpha$ . We simulated the reflection intensities of the enantiomorph A for LCP and RCP incident waves with the variation of the structural variable  $\alpha$  at different wavelengths in Figure 6a. The changing trends of the reflection intensity at different wavelengths are different for LCP incident waves, while they are similar for RCP incident waves. Thus, our approach can be used to realize the spin- and wavelength-selective gray imaging. A gray image of a Rubik's cube (displayed in Figure 6b) is designed to make a verification. The designed image is composed of six basic unit cells of enantiomorph A with different  $\alpha$ . With the utilization of unit cells #2 and #4, the intensity distribution in the image will be different at 1300, 1400, and 1500 nm (as show in Figure 6a), resulting in different gray images of the Rubik's cube.

Figure 6c represents the calculated data of the gray imaging under LCP illumination at 1300, 1400, and 1500 nm, respectively. It is clearly demonstrated that the gray image of the Rubik's cube is different at different wavelengths. The corresponding experimental results in Figure 6d, which were captured under the illumination of a bromine tungsten lamp with different wavelength filters, are in good agreement with the calculated results. The experimental results also verify that the Rubik's cube cannot be observed under RCP illumination because the reflection intensity of RCP illumination keep constant with the variation of the angle  $\alpha$ . Moreover, the gray imaging under broadband illumination is quite different from that at the operation wavelength of enantiomorph A. We anticipate this key feature will provide a new approach for optical information hiding. In general, our approach is a good alternative for the realization of spin- and wavelength-selective gray imaging, which can be used for optical encryption and information hiding.

Another outstanding advantage of the proposed chiral mirrors is that the operation wavelength can be continuously tuned in the wavelength range from 1000 to 2000 nm by changing structural variable  $\beta$ . We can realize the wavelength-selective spin detection with spin-selective reflection by constructing an optical chip, which is shown in Figure 7a. The proposed optical chip consists of ten different areas. The first and second row are composed of unit cells of enantiomorph A and B with different structural variable  $\beta$ , respectively. We calculated the reflection difference  $\Delta r = r_{\text{LCP}} - r_{\text{RCP}}$  of the ten areas for the designed optical chip under LCP and RCP illuminations at different wavelengths in Figure 7b. The operation wavelengths of the areas in each column in the optical chip are the same while their spin-selective optical responses are opposite. The operation wavelengths of the areas in each row in the optical chip

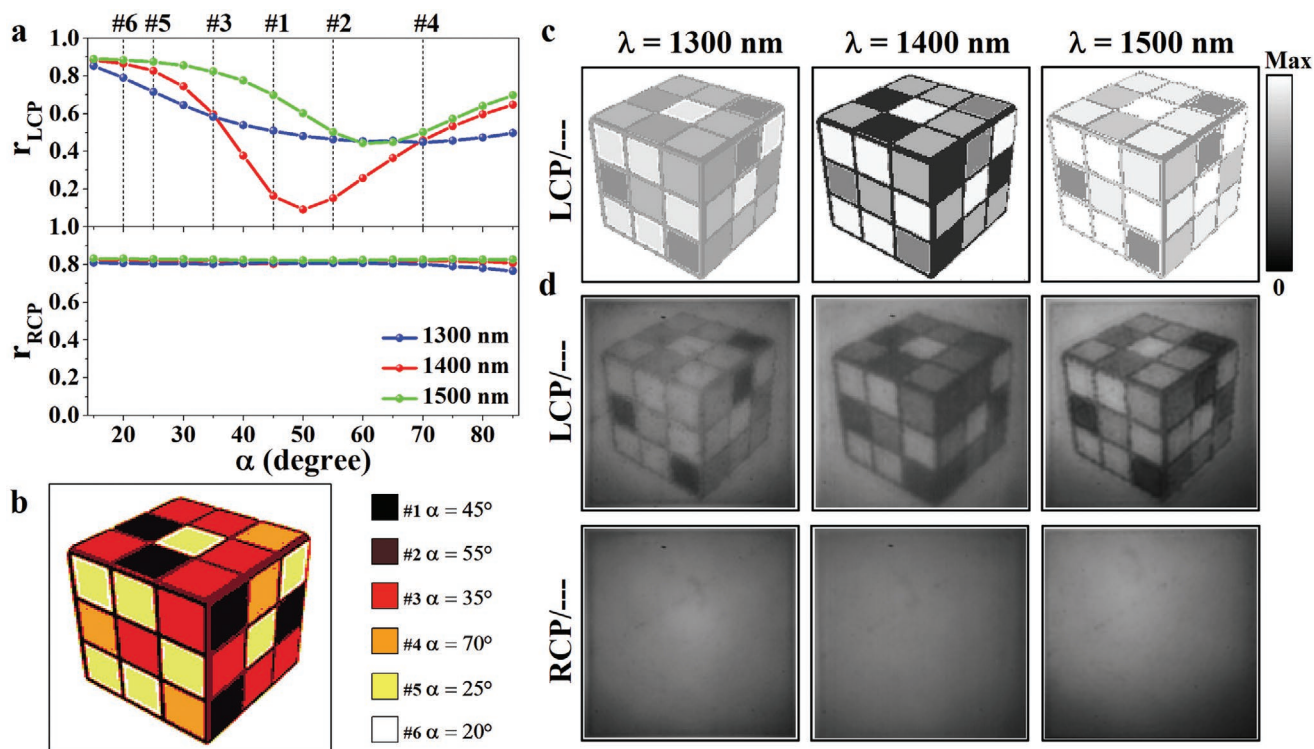


**Figure 6.** Spin and wavelength-selective gray imaging with the designed chiral mirrors. a) Simulated results of the variation of the reflection intensity of the enantiomorph A with the changing of the structural variable  $\alpha$  at wavelength of 1300, 1400, and 1500 nm, where  $r_{LCP} = r_{LL} + r_{RL}$  and  $r_{RCP} = r_{RR} + r_{LR}$ . b) Design schematic of the spin- and wavelength-selective gray image of a Rubik's cube. The designed gray image has 145 pixels in both  $x$ - and  $y$ -directions, and each pixel consists of one of six basic unit cells with different structural variable  $\alpha$ . c) Calculated results of the gray image with LCP illumination at 1300, 1400, and 1500 nm. d) Experimental results of the gray image under LCP and RCP illuminations at 1300, 1400, and 1500 nm. The name and representations of the Rubik's Cube are used by permission of Rubik's Brand Ltd. www.rubiks.com.

have a redshift with the increasing of the angle  $\beta$  while their spin-selective optical responses are the same. The insets of Figure 7b give the experimental results of the optical chip for

the wavelength-selective spin detection. These images were captured under the illumination of a supercontinuum laser. The experimental results clearly validate that the reflection intensity

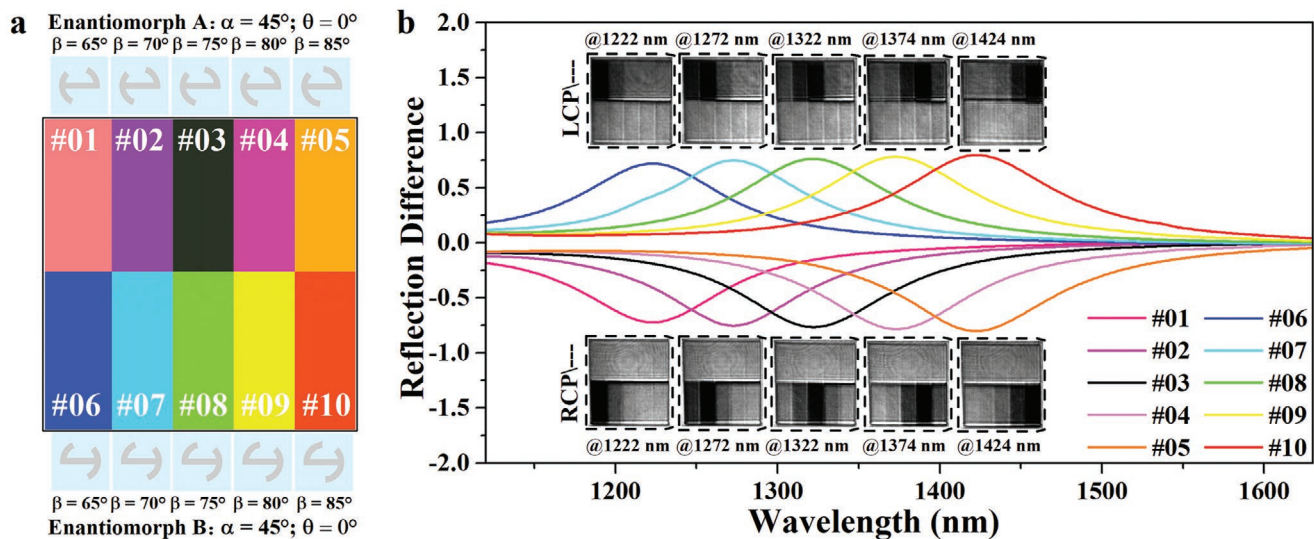


**Figure 8.** Wavelength-selective spin detection with the designed chiral mirrors. a) Design schematic of the optical chip for wavelength-selective spin detection. The designed chip has ten different area in which there are 30 pixels in  $x$ -direction and 75 pixels in  $y$ -direction, and each pixel consists of one of the ten basic unit cells in which the chiral optical response and the structural variable  $\beta$  are different. b) Calculated results of the reflection difference  $\Delta r = r_{LCP} - r_{RCP}$  of the ten areas and experimental results of the wavelength-selective spin detection with the designed chip under LCP and RCP illuminations at different wavelengths.

distributions of the designed optical chip are different for different spins at different wavelengths. For example, for LCP illumination at 1272 nm, the area #02 barely reflects optical waves while the areas #01 and #03 partially reflect optical waves and the other areas almost completely reflect optical waves. Thus, based on the reflection intensity distribution of the optical chip, not only the spin of the optical waves but also the wavelength of the illumination can be obtained. The current proposed optical chip is a simple example to verify the wavelength-selective spin detection. By designing more areas and utilizing the deep-learning technology,<sup>[48,49]</sup> we believe that both the working waveband and the accuracy of spin detection will be dramatically improved.

Realizing spin-selective multidimensional manipulation of optical waves based on metasurfaces plays a key role in nanophotonics and spin optics. Recently, spin-selective phase and amplitude manipulation of optical waves has been realized in dielectric metasurfaces, which significantly expanded the application range of metasurfaces.<sup>[23,24,28,29]</sup> However, manipulation of amplitude and phase of optical waves in these approaches can only be realized in several fixed wavelengths. Although the operation wavelength can be adjusted by scaling the structural parameters, the adjustable range is limited and the high order diffractions and extra noise will appear as a consequence. Moreover, the optical responses of the structures need to be further optimized to control the amplitude and phase of optical waves. Thus, these approaches have some disadvantages in modulation depth, operation wavelength, working efficiency, optimization time, and universal applicability. A versatile platform for the realization of spin-selective amplitude and phase manipulation of optical waves with a large and continuous wavelength agility and a large modulation depth, namely spin-selective full-dimensional manipulation of optical waves, is still highly desirable.

Here, we have proposed a new design principle of chiral mirror to realize the spin-selective full-dimensional manipulation of optical waves. We proposed two chiral mirrors with opposite spin-selective optical responses in which the reflection difference for incident waves with opposite circular polarization states are over 78% with near-perfect extinction of one circular-polarized illumination. With both qualitative and quantitative theoretical analysis, we proved that the spin-selective reflection in the proposed chiral mirrors originates from the spin-selective generation of a pair of antiparallel currents within the nanostructures. Based on this underlying physics, we revealed the direct relationship between the structural parameters of the designed chiral mirrors and each optical dimension, as a result, providing a method to attribute three optical dimensions (amplitude, phase and operation wavelength) to three different structural variables. By involving two chiral mirrors with opposite spin-selective responses and simply changing three structural variables of the chiral mirrors, the proposed design principle can arbitrarily and independently empower the spin-selective manipulation of amplitude, phase, and operation wavelength of circular-polarized waves with a large modulation depth. With experimental validation, we further proved that the proposed chiral mirrors can be used not only in the applications based on spin-selective phase manipulation of optical waves, but also in the areas of optical encryption, imaging,

and detection. Our work overcomes the drawbacks in previous chiral mirrors and provides a simple solution for the full implementation of spin-selective manipulation of optical waves. We firmly believe that the spin-selective optical functionalities and applications that are not validated in our work can be easily realized by following the proposed design principle.

## Experimental Section

**Sample Fabrication:** The proposed aluminum chiral mirror was fabricated by electron-beam lithography (EBL), and aluminum (Al) lift-off process. A 200 nm thick Al film was initially deposited onto a microscope slide glass by using an electron-beam evaporator (Temescal BJD-2000). A 180 nm thick SiO<sub>2</sub> layer was subsequently deposited onto the sample by using plasma enhanced chemical vapor deposition (PECVD). After that, a 200 nm thick positive electron-beam resist of ZEP520A was spin-coated, and then the structure pattern was exposed using an EBL system (RAITH 150) at 30 keV. After the exposure, the sample was developed in *n*-amyl acetate for 60 s, rinsed with isopropyl alcohol, and then blown dry using nitrogen. A 70 nm thick Al film was subsequently deposited by using an electron-beam evaporator (Temescal BJD-2000). After the resist was removed by means of a ZEP remover (ZDMAC), the Al chiral mirror were created.

**Numerical Simulations:** Numerical simulations were conducted using finite differential time domain methods. The optical constants of Al were taken from Palik's handbook and the refractive index of SiO<sub>2</sub> was taken as 1.47.<sup>[50]</sup> The periodic boundary conditions were set in the *x* and *y* directions representing a periodical structure, and waveguide ports boundary was defined in the *z* direction for light incidence and transmission while the excitation source was either a left- or a right-handed circularly polarized plane wave.

**Experimental Measurement:** The experimental measurement of the reflection spectra for the proposed Al chiral mirror was based on a custom-built optical setting (see Figure S9, Supporting Information). White light from a bromine tungsten lamp (Zolix, LSH-150) in the normal direction was used as the light source, and the light beam was collimated by a fiber collimator. Then the collimated beam passed through an aperture, a broadband polarizer (Thorlabs, LPNIR050-MP2), and an achromatic quarter-wave plate (B. Halle Nachfl) to generate a circular-polarized beam. The circular-polarized beam then passed through a broadband unpolarized prism (MFOPT, OQNP20N-NIR-3) and was focused on the sample with an objective (Sigma NIR plan apo 20×, NA = 0.45). The output light from the sample was collected with the same objective. Then the collected beam passed through a 4f-system formed by two lenses with an aperture set near the focus that is used to adjust the spot size of the light. Then the collected beam passed through an achromatic quarter-wave plate (B. Halle Nachfl) and a broadband polarizer (Thorlabs, LPNIR050-MP2). The beam then passed through a broadband unpolarized prism (MFOPT, OQNP20N-NIR-3) and collected by an optical spectrum analyzer (Zolix, Omni-λ3007) via a fiber coupler and an InGaAs camera (HAMAMATSU InGaAs C10633). The data of reflection spectra were acquired with the software of the optical spectrum analyzer. Al mirror was used as the reference for measuring the reflectance. By utilizing the narrow-band interference filters (MFOPT, M-130FS20-25, M-140FS20-25, and M-150FS20-25), the images were taken in the software of the InGaAs camera. Part of the images were measured based on the other custom-built microscopy. The light source was a supercontinuous laser (NKT SuperK EXR-20), and the laser beam was collimated by a fiber collimator. Two lenses were used to expand the collimated beam. Then the collimated beam passed through a broadband polarizer (Thorlabs, LPNIR050-MP2) and an achromatic quarter-wave plate (B. Halle Nachfl) to generate a circular-polarized beam. The circular-polarized beam then passed through a broadband unpolarized prism (MFOPT, OQNP20N-NIR-3) and was focused on the sample with an objective (Sigma NIR plan apo 20×, NA = 0.45). The output light from the sample was collected with the same

objective. Then the beam passed through a broadband unpolarized prism (MFOPT, OQNP20N-NIR-3), an achromatic quarter-wave plate (B. Halle Nachfl) and a broadband polarizer (Thorlabs, LPNIR050-MP2). The beam was collected with an InGaAs camera (HAMAMATSU InGaAs C10633). The images were then taken in the software of the CCD camera.

## Supporting Information

Supporting Information is available from the Wiley Online Library or from the author.

## Acknowledgements

This work was supported by the National Key Research and Development Program of China (2016YFA0301102 and 2017YFA0303800), the National Natural Science Fund for Distinguished Young Scholar (11925403), the National Natural Science Foundation of China (11974193, 11904181, 11904183, 91856101, and 11774186), Natural Science Foundation of Tianjin for Distinguished Young Scientists (18JCQJC45700), the National Postdoctoral Program for Innovative Talents (BX20180148), the China Postdoctoral Science Foundation (2018M640224 and 2018M640229), and 111 Project (B07013). The work was partly performed at the ACT node of the Australian National Fabrication Facility.

## Conflict of Interest

The authors declare no conflict of interest.

## Keywords

chiral mirrors, full-dimensional light manipulation, optical encryption, spin detection, spin-selective light manipulation

Received: December 5, 2019

Revised: March 25, 2020

Published online:

- [1] D. Neshev, I. Aharonovich, *Light: Sci. Appl.* **2018**, *7*, 58.
- [2] F. Capasso, *Nanophotonics* **2018**, *7*, 953.
- [3] S. Chen, Z. Li, W. Liu, H. Cheng, J. Tian, *Adv. Mater.* **2019**, *31*, 1802458.
- [4] K. Y. Bliokh, F. J. Rodríguez-Fortuño, F. Nori, A. V. Zayats, *Nat. Photonics* **2015**, *9*, 796.
- [5] S. Xiao, J. Wang, F. Liu, S. Zhang, X. Yin, J. Li, *Nanophotonics* **2016**, *6*, 215.
- [6] M. Pu, X. Li, X. Ma, Y. Wang, Z. Zhao, C. Wang, C. Hu, P. Gao, C. Huang, H. Ren, X. Li, F. Qin, J. Yang, M. Gu, M. Hong, X. Li, *Sci. Adv.* **2015**, *1*, e1500396.
- [7] Y. Guo, M. Pu, Z. Zhao, Y. Wang, J. Jin, P. Gao, X. Li, X. Ma, X. Luo, *ACS Photonics* **2016**, *3*, 2022.
- [8] M. Schäferling, *Chiral Nanophotonics*, Springer Series in Optical Sciences, Vol. 205, Springer International Publishing, Cham, Switzerland **2017**.
- [9] Y. Luo, C. Chi, M. Jiang, R. Li, S. Zu, Y. Li, Z. Fang, *Adv. Opt. Mater.* **2017**, *5*, 1700040.
- [10] M. Qiu, L. Zhang, Z. Tang, W. Jin, C. W. Qiu, D. Y. Lei, *Adv. Funct. Mater.* **2018**, *28*, 1803147.
- [11] J. T. Collins, C. Kuppe, D. C. Hooper, C. Sibia, M. Centini, V. K. Valev, *Adv. Opt. Mater.* **2017**, *5*, 1700182.
- [12] Y. Luo, C. Chi, M. Jiang, R. Li, S. Zu, Y. Li, Z. Fang, *Adv. Opt. Mater.* **2017**, *5*, 1700040.
- [13] M. Khorasaninejad, W. T. Chen, A. Y. Zhu, J. Oh, R. C. Devlin, D. Rousso, F. Capasso, *Nano Lett.* **2016**, *16*, 4595.
- [14] Y. Bao, Q. Jiang, Y. Kang, X. Zhu, Z. Fang, *Light: Sci. Appl.* **2017**, *6*, e17071.
- [15] D. Wen, F. Yue, G. Li, G. Zheng, K. Chan, S. Chen, M. Chen, K. F. Li, P. W. H. Wong, K. W. Cheah, E. Y. B. Pun, S. Zhang, X. Chen, *Nat. Commun.* **2015**, *6*, 8241.
- [16] L. Jin, Z. Dong, S. Mei, Y. F. Yu, Z. Wei, Z. Pan, S. D. Rezaei, X. Li, A. I. Kuznetsov, Y. S. Kivshar, J. K. W. Yang, C.-W. Qiu, *Nano Lett.* **2018**, *18*, 8016.
- [17] M. Kenney, S. Li, X. Zhang, X. Su, T. T. Kim, D. Wang, D. Wu, C. Ouyang, J. Han, W. Zhang, H. Sun, S. Zhang, *Adv. Mater.* **2016**, *28*, 9567.
- [18] S. Yang, Z. Liu, S. Hu, A. Z. Jin, H. Yang, S. Zhang, J. Li, C. Gu, *Nano Lett.* **2019**, *19*, 3432.
- [19] Z. Li, W. Liu, H. Cheng, S. Chen, J. Tian, *Sci. Rep.* **2017**, *7*, 8204.
- [20] J. Liu, Z. Li, W. Liu, H. Cheng, S. Chen, J. Tian, *Adv. Opt. Mater.* **2016**, *4*, 2028.
- [21] D. Ma, Z. Li, Y. Zhang, W. Liu, H. Cheng, S. Chen, J. Tian, *Opt. Lett.* **2019**, *44*, 3805.
- [22] Z. Li, W. Liu, H. Cheng, J. Liu, S. Chen, J. Tian, *Sci. Rep.* **2016**, *6*, 35485.
- [23] Z. Ma, Y. Li, Y. Li, Y. Gong, S. A. Maier, M. Hong, *Opt. Express* **2018**, *26*, 6067.
- [24] F. Zhang, M. Pu, X. Li, P. Gao, X. Ma, J. Luo, H. Yu, X. Luo, *Adv. Funct. Mater.* **2017**, *27*, 1704295.
- [25] W. Liu, Z. Li, Z. Li, H. Cheng, C. Tang, J. Li, S. Chen, J. Tian, *Adv. Mater.* **2019**, *31*, 1901729.
- [26] L. Huang, H. Mühlenbernd, X. Li, X. Song, B. Bai, Y. Wang, T. Zentgraf, *Adv. Mater.* **2015**, *27*, 6444.
- [27] R. C. Devlin, A. Ambrosio, N. A. Rubin, J. B. Mueller, F. Capasso, *Science* **2017**, *358*, 896.
- [28] Y. Bao, Y. Yu, H. Xu, C. Guo, J. Li, S. Sun, Z. K. Zhou, C. W. Qiu, X. H. Wang, *Light: Sci. Appl.* **2019**, *8*, 95.
- [29] A. C. Overvig, S. Shrestha, S. C. Malek, M. Lu, A. Stein, C. Zheng, N. Yu, *Light: Sci. Appl.* **2019**, *8*, 92.
- [30] I. J. Hodgkinson, M. Arnold, M. W. McCall, A. Lakhtakia, *Opt. Commun.* **2002**, *210*, 201.
- [31] M. Pu, P. Chen, Y. Wang, Z. Zhao, C. Huang, C. Wang, X. Ma, X. Luo, *Appl. Phys. Lett.* **2013**, *102*, 131906.
- [32] E. Plum, N. I. Zheludev, *Appl. Phys. Lett.* **2015**, *106*, 221901.
- [33] L. Kang, S. P. Rodrigues, M. Taghinejad, S. Lan, K. T. Lee, Y. Liu, D. H. Werner, A. Urbas, W. Cai, *Nano Lett.* **2017**, *17*, 7102.
- [34] Z. Wang, H. Jia, K. Yao, W. Cai, H. Chen, Y. Liu, *ACS Photonics* **2016**, *3*, 2096.
- [35] L. Ouyang, W. Wang, D. Rosenmann, D. A. Czaplewski, J. Gao, X. Yang, *Opt. Express* **2018**, *26*, 31484.
- [36] M. Pan, Q. Li, Y. Hong, L. Cai, J. Lu, M. Qiu, *Opt. Express* **2018**, *26*, 17772.
- [37] L. Jing, Z. Wang, Y. Yang, B. Zheng, Y. Liu, H. Chen, *Appl. Phys. Lett.* **2017**, *110*, 231103.
- [38] W. Li, Z. J. Coppens, L. V. Besteiro, W. Wang, A. O. Govorov, J. Valentine, *Nat. Commun.* **2015**, *6*, 8379.
- [39] L. Jing, Z. Wang, R. Maturi, B. Zheng, H. Wang, Y. Yang, L. Shen, R. Hao, W. Yin, E. Li, H. Chen, *Laser Photon. Rev.* **2017**, *11*, 1700115.
- [40] H. X. Xu, G. Hu, Y. Li, L. Han, J. Zhao, Y. Sun, F. Yuan, G.-M. Wang, Z.-H. Jiang, X. Ling, T.-J. Cui, C.-W. Qiu, *Light: Sci. Appl.* **2019**, *8*, 3.
- [41] Q. Wang, E. Plum, Q. Yang, X. Zhang, Q. Xu, Y. Xu, J. Han, W. Zhang, *Light: Sci. Appl.* **2018**, *7*, 25.
- [42] W. Ma, F. Cheng, Y. Liu, *ACS Nano* **2018**, *12*, 6326.
- [43] Z. Li, D. Rosenmann, D. A. Czaplewski, X. Yang, J. Gao, *Opt. Express* **2019**, *27*, 28313.
- [44] S. Q. Li, W. Song, M. Ye, K. B. Crozier, *ACS Photonics* **2018**, *5*, 2374.

- [45] N. Papasimakis, V. A. Fedotov, V. Savinov, T. A. Raybould, N. I. Zheludev, *Nat. Mater.* **2016**, *15*, 263.
- [46] P. C. Wu, C. Y. Liao, V. Savinov, T. L. Chung, W. T. Chen, Y. W. Huang, P. R. Wu, Y. H. Chen, A. Q. Liu, N. I. Zheludev, D. P. Tsai, *ACS Nano* **2018**, *12*, 1920.
- [47] G. C. Li, Y. L. Zhang, J. Jiang, Y. Luo, D. Y. Lei, *ACS Nano* **2017**, *11*, 3067.
- [48] A. Tittl, A. Leitis, M. Liu, F. Yesilkoy, D. Y. Choi, D. N. Neshev, Y. S. Kivshar, H. Altug, *Science* **2018**, *360*, 1105.
- [49] Z. Liu, S. Yan, H. Liu, X. Chen, *Phys. Rev. Lett.* **2019**, *123*, 183902.
- [50] E. D. Palik, *Handbook of Optical Constants of Solids*, Academic Press, New York **1998**.